Effects of substrate and post-deposition annealing on structural and optical properties of $(ZnO)_{1-x}(GaN)_x$ films

V. S. Olsen[1], C. Bazioti[1], G. Baldissera[2], A. Azarov[1], Ø. Prytz[1],

C. Persson[1,2], B. G. Svensson[1], A. Yu. Kuznetsov[1], and L. Vines[1]

[1]*Department of Physics, Center for Materials Science and Nanotechnology,*
University of Oslo, P.O.Box 1048, Blindern, N-0316 Oslo, Norway and
[2]*Department of Materials Science and Engineering,*
Royal Institute of Technology, SE-100 44 Stockholm, Sweden.

(Dated: April 9, 2019)

The structural and optical properties of magnetron sputtered thin films of $(ZnO)_{1-x}(GaN)_x$ deposited on zinc oxide, sapphire and silicon oxide are studied as a function of strain accumulation and post-deposition anneals at 600 - 800°C. For the experimental conditions studied, we found that different amounts of tensile strain accumulated in the samples practically does not affect the strong bandbowing effect, i.e. optical bandgap, observed in the as-deposited alloys. In its turn, post-deposition annealing results in a reduction of the tensile strain and dislocation density in the films, as measured by both X-ray diffraction and transmission electron microscopy, corroborating an increase in the crystal quality. In addition, the grain size was found to increase with annealing temperature, e.g mean values of 20 nm up to 50 nm were measured for the alloys with $x = 0.15$. Meanwhile, the full-width at half maximum of the (0002) x-ray diffraction reflection increases with annealing temperature, but with only a small increase in bandgap energies for the $x = 0.15$ sample. However, this observation was explained combining the experimental data and first-principles calculations based on density functional theory, showing that the increase in the amount of Ga-N bonds lowers the total energy of the system. As such, we conclude that the thermal treatments increase the Ga-N ordering, resulting in several contributions or a widening of the diffraction peaks.

I. INTRODUCTION

Controlling the functional properties is essential when developing novel semiconductor materials. ZnO and GaN are wide-bandgap semiconductors, with bandgap energies of ~3.3 eV and ~3.4 eV, respectively, at room temperature, making them applicable for optoelectronic devices such as light emitting diodes (LEDs) and lasers, solar blind detectors, and transparent conducting oxides[1]. When alloying ZnO and GaN in a $(ZnO)_{1-x}(GaN)_x$ alloy, a narrowing of the bandgap, E_g, has been found to occur, i.e a so-called bandbowing effect, well into the visible spectrum[2]. The origin of this bandbowing effect is still under debate, where orbital-repulsion within the valence band[3–6] and type-II band alignment[7,8] have both been suggested as plausible candidates. This bandgap narrowing has been exploited for water-splitting applications[9–11], but is also a potential candidate for various optoelectronic applications as the alloy has been successfully fabricated as highly crystalline thin films as well[12,13].

Experimentally, $(ZnO)_{1-x}(GaN)_x$ have mainly been grown using solid solution synthesis and for Ga and N rich compositions[10,11,14,15]. Shet et al. reported on sputtered alloy samples deposited on tin oxide substrates[16], while Olsen et al. demonstrated alloyed films deposited by magnetron sputtering on sapphire substrates with up to 20% Ga and N incorporation[12]. Sapphire substrates were also used for depositing thin films utilizing pulsed-laser-deposition in the work by Yang et al[13]. However, the influence of the substrate on the structural and optical properties (in particular, the influence of the lat-tice mismatch and E_g properties) remains unexplored. In addition, the optical properties have been found theoretically to be affected by the local environment of the atoms, i. e. the structural configuration[3,17]. There is on the other hand little experimentally obtained results exploring the effects of different structural configurations. Sputter deposition techniques result in films that are out of thermal equilibrium, thus post-deposition anneals may modify the material towards more thermally stable configuration.

In the present work, we have investigated the structural and optical dependencies of $(ZnO)_{1-x}(GaN)_x$ thin films with $0 \leq x \leq 0.2$ deposited on ZnO, Al_2O_3 and SiO_2, representing lattice-matched, lattice-mismatched and amorphous substrates, respectively. Further, the influence of post-deposition annealing in nitrogen atmosphere on the structural and optical properties of the films deposited on the sapphire substrates was investigated, monitoring the evolution while shifting the balance towards thermal equilibrium.

II. EXPERIMENTAL DETAILS

$(ZnO)_{1-x}(GaN)_x$ thin films were deposited on different lattice matched substrates, specifically O-faced ZnO, c-plane sapphire and amorphous quartz, using a Moorfield Minilab magnetron sputtering system with separate ZnO (99.999% purity) and GaN (99.99% purity) 3 inch targets. The ZnO and sapphire substrates were cleaned by annealing in oxygen atmosphere for one hour at 1150 °C, while the quartz substrates were cleaned using the

RCA process, before the samples were loaded into the sputter chamber. The base pressure prior to deposition was below 2×10^{-6} Torr, while the pressure during deposition was kept at 7 mTorr. The substrate temperature was kept at 400°C and the sample stage was rotated at 11 rpm to ensure good film uniformity. A pre-sputtering cleaning was carried out for 20 minutes before deposition to remove surface impurities from the targets. During the co-sputtering process, where the two targets are running simultaneously, the composition was controlled by applying different voltages to the targets, in addition to controlling the gas flows of N_2 and Ar in the chamber. For instance, to obtain $x = 0.15$ (see Table I), 30W and 20W were applied to the ZnO and GaN targets, respectively, while gas flows of 12.5 SCCM Ar and 5 SCCM N_2 were kept constant during deposition. The deposition times varied for the respective composition in order to obtain films with thicknesses of ~1.5 μm, as measured by ellipsometry, see Table I.

The Ga and N content in the alloy films were measured using scanning electron microscopy (SEM) in energy dispersive X-ray spectroscopy (EDS) mode. Utilizing secondary ion mass spectrometry (SIMS), the Ga and N concentrations were also measured as a function of film-depth by using a Cameca IMS 7f microanalyzer with either 15 keV Cs^+ or 10 keV O_2^+ ions as the primary beam. The depth of the sputtered crater was measured by a Veeco Dektak 8 stylus profilometer. Assuming a uniform and time-independent erosion rate, the measured crater depth was used to convert sputtering time to sample depth. Ga and N ion implanted reference samples were used to convert the recorded secondary ion intensities to concentration.

X-ray diffraction (XRD) characterization was made utilizing the Bruker AXS D8 Discover system. The x-ray source was Cu Kα ($\lambda = 1.5406$ Å), and a Ge (220) double bounce monochromator was implemented to filter out the Kα_2 signal ($\lambda = 1.5444$ Å). The instrumental broadening of the diffraction peaks of 0.008° is included in the standard error bar while analyzing the results. Transmission measurements were carried out using a Shimadzu SolidSpe-3700 DUV spectrophotometer. The wavelength range of this instrument is 175-2600 nm, with 0.1 nm resolution.

Rutherford backscattering spectroscopy (RBS) analysis of the thin films were realized using the National Electrostatics Corporation (NEC) tandem ion accelerator employing 1.62 MeV He$^+$ ions, incident along the [0001] direction. The backscattered beam was analyzed at an angle of 165° with respect to the incident beam.

Transmission electron microscopy (TEM) thin foil preparation for cross-sectional observations was performed by mechanical grinding using the tripod wedge polishing method in the Allied Multiprep, followed by Ar$^+$ ion milling in the Gatan PIPS II. Finally the samples were plasma cleaned using a Fichione Model 1020 plasma cleaner in order to minimize carbon contamination. (Scanning) TEM ((S)TEM) observations were per-

formed in a probed-corrected FEI Titan G2 60-300 microscope, operated at 300 kV.

III. COMPUTATIONAL METHODS

The crystalline structures of $(ZnO)_{1-x}(GaN)_x$ alloys were also determined theoretically using the Perdew-Burke-Ernzerhof (PBE) generalized gradient approximation[18,19] within the density functional theory (DFT), as provided by the VASP software package[20,21]. A 72-atom unit cell structure was modeled for the alloys, where the Ga-N concentration of $x = 14/72 \approx 0.194$ were obtained by replacing seven Zn-O pairs. We choose different configurations for this concentration, for which we calculate the differences in formation energies. Although PBE does not generate accurate absolute values of the bandgap energy, we can still analyze if various alloy configuration yield changes in the gap energies. With a cut-off energy of 700 eV, the relaxation was carried out alternating between volume and atom position relaxation until the final force in the atoms were smaller than 5 meV/Å. Thereafter, a cut-off energy of 400 eV was used in the PBE calculations together with a Γ-centered 8×8×8 **k**-mesh in the final calculations.

IV. RESULTS AND DISCUSSION

$(ZnO)_{1-x}(GaN)_x$ thin films with x ranging from 0 to 0.20 were manufactured using co-sputtering deposition, as previously reported[12]. The composition, x, is taken twice the measured Ga content using SEM, see Table I. In addition, the $x = 0.15$ thin film was measured using SIMS, both to ensure that there were no large variations in Ga- and N concentration as a function of the film depth, as well as to have a supporting result for the composition, x, by averaging the Ga- and N concentrations over the film thickness. The films were found to be highly crystalline and yield a good heteroepitaxial relationship to the sapphire substrate. The optical absorption onset of the films shift towards lower energies with increasing GaN content x, as expected due to E$_g$ lowering. Hence, in the following a redshift of the optical onset will be interpreted as a decrease in E$_g$.

A. Influence of different lattice-matched substrates

$(ZnO)_{1-x}(GaN)_x$ thin films with x varying from 0.02 to $x = 0.20$ were deposited on ZnO (O-faced), c-sapphire and quartz substrates, representing a lattice-matched, a lattice-mismatched and an amorphous substrate, respectively. Using the (0002) XRD reflection of the $(ZnO)_{1-x}(GaN)_x$ films, the c-lattice constants were calculated and plotted as a function of GaN content, x, for the films grown on the different lattice-matched substrates, as shown in Figure 1. The lattice constants of the alloy,

TABLE I: Survey of the samples prepared for this study, together with the growth parameters, as well as the measured thicknesses using ellipsometry.

Conc.			Power	Power	Flow	Flow	Thickness	Time
x	Ga	N	ZnO	GaN	Ar	N_2		
	at.%	at.%	(W)	(W)	(SCCM)	(SCCM)	(nm)	(min)
0	0	0	30	0	12.5	0	1380	1440
0.02	1.1±0.1	3.0±0.3	30	7	12.5	0.7	1110	1440
0.07	3.5±0.2	3.4±0.3	30	10	12.5	0.7	1690	1440
0.15	7.5±0.4	5.7±0.4	30	20	12.5	5	1330	1200
0.19	9.5±0.5	6.5±0.5	20	20	10	20	1880	1800
0.20	10.0±0.5	7.9±0.5	30	30	10	20	1290	1200

both a and c, are expected to follow Vegard's law[22], decreasing linearly from ZnO to GaN, where the expected linear decrease in c-lattice constant is represented by a dashed line in Figure 1. The expected decrease in a-lattice constant yields an increase in the in-plane lattice mismatch of the $(ZnO)_{1-x}(GaN)_x$ alloy on ZnO substrate from 0 - 2.8% with increasing GaN content, x. The same in-plane lattice mismatch will vary from 31.7 - 33.6% when deposited on c-sapphire substrate, assuming that there is no in-plane rotation of the film's unit cell with respect to the the unit cell of the substrate. $(ZnO)_{1-x}(GaN)_x$ films were found, utilizing TEM, to exhibit 30° rotation of the unit cell with respect to that of the c-sapphire substrate[12]. This orientation relationship is common since it results in a favorable mismatch (close to 18%[23–25] for ZnO on c-sapphire).

The strain along the c-axis in a thin film is defined as $\epsilon_c = (c - c_0)/c_0$, where c is the measured c-parameter, and c_0 is a reference lattice parameter[26]. Therefore, for a specific composition, x, ϵ_{c_x} may be estimated as $\epsilon_{c_x} = (c_{measured_x} - c_{vegard_x})/c_{vegard_x}$ where $c_{measured_x}$ is the measured c-parameter, and c_{vegard_x} is an approximated c-parameter for that composition, x, predicted by Vegard's law. As can be seen in Figure 1, the measured c-lattice constants of all alloy thin films are larger than those predicted by Vegard's law, indicating the accumulation of tensile strain. This situation is observed regardless of the substrate used, but the magnitude of the strain is substrate-dependent. The films deposited on the O-faced ZnO substrates exhibit the lowest tensile strain, with the c-lattice constant slightly decreasing from $x = 0.02$ to 0.15. Further, the films deposited on c-sapphire substrates yield higher tensile strain. For the $x = 0.02$, the c-lattice constant is close to that of the film deposited on O-faced ZnO. Notably, instead of a decrease in c-lattice constant with increasing GaN concentration, as predicted by Vegard's law[22] and observed on the O-faced ZnO substrates, the c-lattice constant increases when incorporating more GaN on c-sapphire substrates. The highest tensile strain is observed in the alloy thin films deposited on the amorphous quartz substrates. Also in these films, an increase in the c-lattice constant
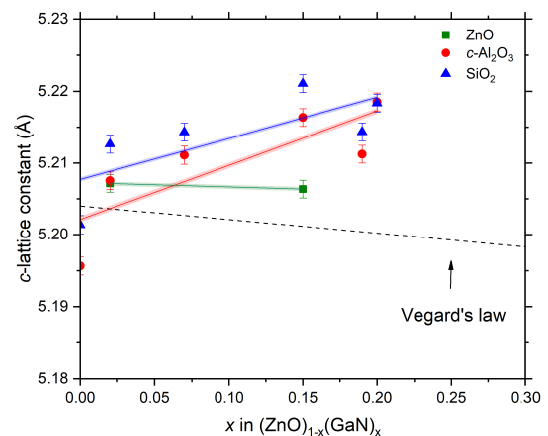
is observed for increasing GaN content.

FIG. 1: c-lattice constants as deduced from the XRD data as a function of GaN concentration, x, for $(ZnO)_{1-x}(GaN)_x$ grown on different substrates. The dashed line illustrates the change in the c-lattice parameter in the alloy as predicted by Vegard's law. Linear fits for the deduced lattice constants for ZnO, Al_2O_3 and SiO_2 are shown as green, red and blue lines respectively, whereas semitransparent areas surrounding the lines are present for better visual representation.

Figure 2 displays the full width at half maximum (FWHM) of the (0002) peak using $\theta/2\theta$ and rocking curve scans. Similar to the measurements of the c-lattice constant, the FWHM of the $\theta/2\theta$ scans (square markers in Figure 2) show the lowest values for the films deposited on O-faced ZnO substrates, while the FWHM increase for the films deposited on c-sapphire and quartz. An increase in FWHM is typically interpreted in terms of a decrease in the grain size, e.g. as calculated by the Scherrer equation[27], and thus as a downturn in crystal quality. Evaluating the rocking curve FWHM data again (triangles in Figure 2), there is a clear trend for the lowest values on the lattice-matched substrate, while
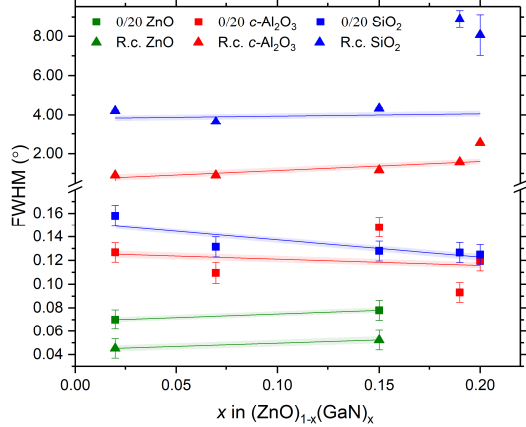
FIG. 2: FWHM values from the $\theta/2\theta$-scans (squares) and rocking curve scans (triangles) for the films deposited on O-faced ZnO (green), c-sapphire (red) and amorphous quartz (blue). Linear fits for $\theta/2\theta$-scans (lines) and rocking curve scans (dashed lines) are shown, in addition semitransparent areas surrounding the fits for better visual representation.

FIG. 3: Tauc plot as constructed from the optical transmission data assuming direct E_g. The filled triangles represent the $x = 0.02$, the empty squares represent the $x = 0.15$, and the films were deposited on ZnO (green), Al_2O_3 (red) and SiO_2 (blue). The dotted lines represent the extension of the linear region of the absorption edge, indicating E_g at the intersect with the energy-axis. The inset shows raw transmittance data as a function of wavelength from the same samples and using the same type of legend.

the films deposited on the amorphous substrate yield the largest FWHM. Notably, the broadening in rocking curve peaks is often related to the increase in dislocation density. Thus, the FWHM data trend indicates an increase in the dislocation density in the films as a function of the substrate mismatch.

Figure 3 is a Tauc plot as constructed from the optical transmission data for $(ZnO)_{1-x}(GaN)_x$ films with $x = 0.02$ and $x = 0.15$ grown on the different substrates; the raw data are included in the inset. The transmittance of the films (inset in Figure 3) deposited on sapphire substrates is somewhat lower than that for the two other substrates since the sapphire substrates were only one-side polished, provoking higher reflection. In contrast to the difference observed for the c-lattice constant and FWHM values, E_g is found to be similar for each alloy composition independently of the substrates used, specifically ~2.9 - 3.1 eV and ~2.4 - 2.5 eV for $x = 0.02$ and $x = 0.15$, respectively. The large Urbach-tail observed for $x = 0.02$, and the smaller Urbach-tail observed for $x = 0.15$, were also independent of the substrate. A large Urbach-tail is interpreted as an increased concentration of localized states within E_g, again indicating that the optical properties of the alloy do not change significantly with the substrate used. Notably, pure ZnO and GaN exhibit bandgaps of ~3.3 eV and ~3.4 eV, respectively, at room temperature.

Summarizing the data of the subsection, the tensile strain and dislocation density occurring in the films depend strongly on the choice of substrate, while the optical properties do not vary significantly with substrate.
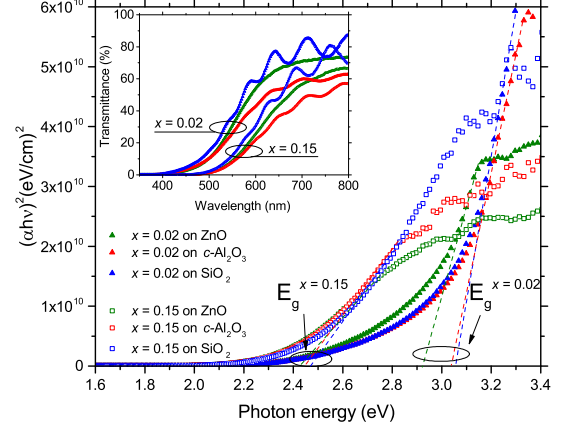
B. Influence of post-deposition annealing

The influence of the post-deposition annealing on the properties of $(ZnO)_{1-x}(GaN)_x$ films deposited on c-Al_2O_3 substrates was investigated using three annealing steps. Each thin film was annealed for one hour in nitrogen atmosphere at 600°C, 700°C and 800°C, with structural and optical characterization after each annealing step. Figure 4 shows the c-lattice constant vs. composition for as-deposited and 800°C annealed samples as measured with XRD (triangles) and HRTEM (circles), compared to the c-lattice constants obtained by Chen et al.[11], who observed an upward bowing of the c-lattice constant as a function of x, in good agreement with our as-grown films. This upward c-lattice constant bowing was also theoretically predicted[4]. The inset in Figure 4 shows the (0002) XRD reflection of the $x = 0.15$ film after deposition (as-grown), as well as after each annealing step. The reflection is shifted towards higher 2θ-angles with annealing temperature, indicating a decrease in c-lattice constant. After the anneals the c-lattice constant comes closer to the values predicted by Vegard's law compared to that of the as-grown samples, indicating a significant lowering of the tensile strain in the films. Sputtering is in general a non-equilibrium process, thus post-deposition annealing is expected to modify the thin films, bringing the alloy towards thermal equilibrium. Indeed, the relaxation observed in Figure 4 can be explained by the increase in atomic mobility, giving the atoms a higher

probability to find more energetically favorable configurations in the lattice, and hence lowering the total energy of the system. Another observation that can be made from Figure 4 is that there is a discrepancy between the c-lattice constants measured with XRD and TEM. The lattice constants obtained from TEM measurements are extracted from smaller, more local areas of the film, whereas the lattice constants measured with XRD are statistically averaged over a larger area. This can imply that for the $x = 0.15$ composition, there is a larger local variation in lattice constants compared to for instance the $x = 0.02$ composition, where the results from the two methods are in more agreement.
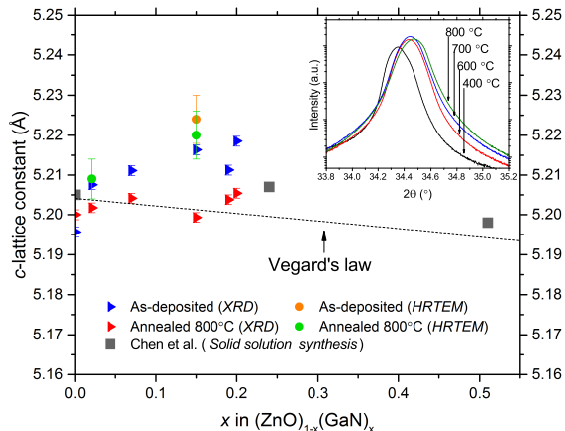
FIG. 4: c-lattice constants as deduced from the XRD data (triangles) and HRTEM (circles) as a function of GaN concentration, x, for $(ZnO)_{1-x}(GaN)_x$ before and after the post-deposition anneals. The results are compared to the lattice constants obtained by Chen et al.[11]. The dashed line illustrates the change in the c-lattice parameter in the alloy as predicted by Vegard's law. The inset shows the (0002) reflection of the $x = 0.15$ film after each annealing step, measured by XRD.

Figure 5 illustrates HAADF (High-angle annular dark-field)-STEM images taken from the upper part of the $x = 0.15$ films (a) before and (b) after the 800°C annealing step. A columnar grain structure is evident and diffraction patterns showed a heteroepitaxial relationship described by $[0001]_{(ZnO)_{1-x}(GaN)_x}//[0001]_{Al_2O_3}$ (out-of-plane) and $[10\bar{1}0]_{(ZnO)_{1-x}(GaN)_x}//[11\bar{2}0]_{Al_2O_3}$ (in-plane), indicating a 30 ° in-plane rotation of the film's unit cell with respect to the unit cell of the substrate. The TEM investigations also revealed a reduced threading dislocation (TD) density after annealing (Figure S1 in Suppl. Mater.), as well as an increase in the width of the grains with mean values of 20 up to 50 nm for as-grown and 800°C annealed samples, respectively. This could be attributed to the grain coalescence during the annealing process, resulting in the formation of larger grains, with fewer defects, and an overall improved crystalline quality.

On the other hand, no clear improvement of the disorder was found after annealing by RBS measurements, see Figure S3 in Suppl. Mater. Nano-sized inclusions of lower density (dark spots), as can be seen in Figure S2 in Suppl. Mater., were also observed after annealing, with the majority of them being located along grain boundaries and TDs.
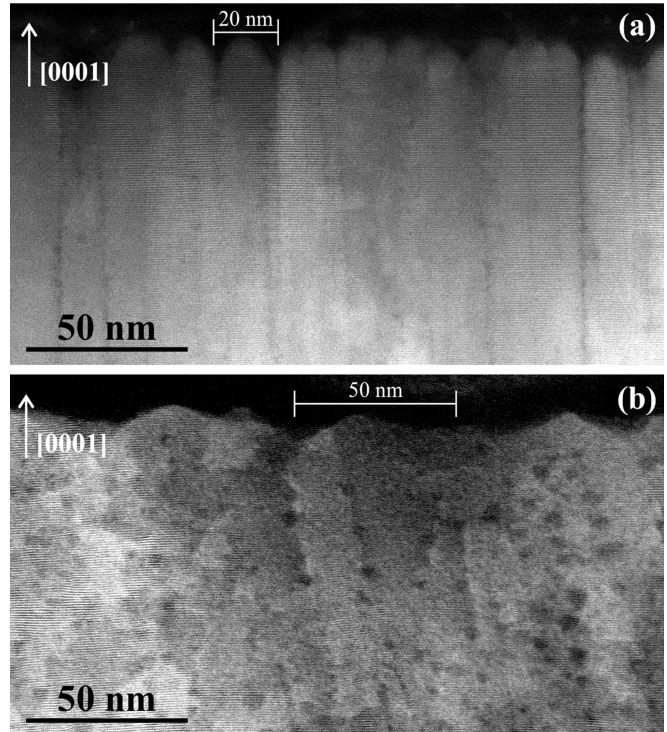

FIG. 5: HAADF-STEM images of the $x = 0.15$ films grown on c-Al$_2$O$_3$ (a) before and (b) after the 800°C thermal annealing step. A clear increase in the grain size is observed after annealing, resulting in an improved overall crystal quality of the films, with lower TD density.

Figure 6 summarizes the FWHM data taken from the (0002) XRD peak for several alloy compositions as a function of annealing temperature. Interestingly, the FWHM for the pure ZnO film decreases with annealing temperature, while the alloy FWHM exhibits an increase. The narrowing of the (0002) XRD reflection for pure ZnO is expected, as post-deposition annealing enhances the overall crystal quality of the film. An ancrease in FWHM, on the other hand, as observed for the alloy can happen either due to (i) a decrease in the crystalline quality, or (ii) because the (0002) peak in the alloy sample may consist of several overlapping contributions evaluated as a single peak.

Considering explanation (i), the measured rocking curve FWHM (see Figure S4 in Suppl. Mater.) show in general a decreasing trend with annealing temperature, a trend especially clear for the low-x compositions, indicating a decrease in dislocation density, as such not support-

ing hypothesis (i). Thus, this argument, together with the considerations of the TEM results above suggest that the crystalline quality increases after post-deposition annealing.
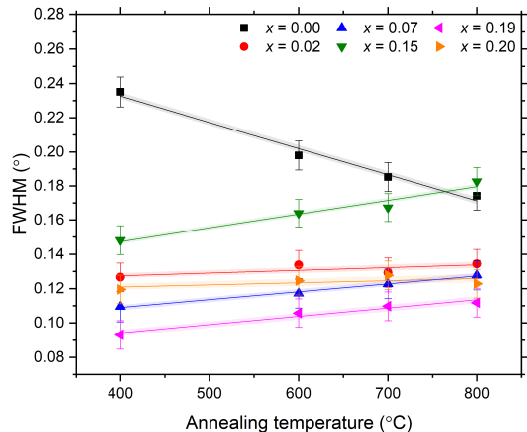

FIG. 6: FWHM of the (0002) peak measured using $\theta/2\theta$ scans as a function of post-deposition annealing temperature for different alloy compositions. Linear fits are presented as lines, with a semitransparent area surrounding for better visual representation.

Figure 7 plots the variation of E_g as extracted from the transmission measurements (see Figure S5 in Suppl. Mater.) as a function of annealing temperature, for the samples with different GaN-content. In accordance with previously reported measurements of the as-deposited samples, the measured optical E_g of pure ZnO and $x =$ 0.02 alloy is ~3.3 and ~2.9 eV, respectively, while the higher GaN-content films show E_g energies ~2.4 - 2.5 eV[12]. By monitoring E_g (i.e. onset of optical absorption) after each annealing step there is an unsystematic change for the different compositions. After the 800 °C anneal, there is no large change in E_g for $x = 0.02$, whereas there is a larger spread in E_g for $0.07 \leq x \leq 0.20$. Interestingly, a change in the bandgap is predicted by theory, where a blueshift in the E_g is predicted when the disorder in the alloy decreases, corroborated by an increase in short-range order using Monte Carlo simulations[3,8], whereas Maeda et al.[28] observed a red-shift in the absorption onset with annealing.

One possible explanation for the change in E_g with annealing temperature is increased crystal quality, where non-radiative defects can be annealed out. A reduced concentration of non-radiative contributions results in a steeper slope in the Tauc plots, increasing the absorption onset. A supporting argument for the reduced number of non-radiative contributions was found when E_g was estimated assuming indirect allowed transitions (i.e. r = 1/2 in the Tauc analysis). This estimate resulted in significantly lower E_g, than those from the direct transitions (not shown), but increasing with the annealing temper-
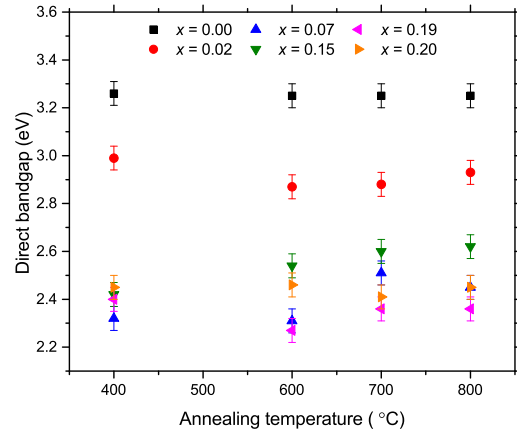

FIG. 7: E_g as a function of annealing temperature for the alloys with different GaN concentration, x. The data are taken from transmission measurements.

ature, approaching those of the direct E_g. This corroborates that non-radiative contributions are annealed out.

Another possible explanation for the evolution of E_g, seen in Figure 7, is related to cluster formation in the alloys. As discussed above, an alternative explanation to the increase in FWHM of the (0002) peak in the $\theta/2\theta$ scans in Figure 6 may be due to the overlapping of several closely located peaks. In particular, this can occur if clusters with different bond lengths are formed during annealing, where clustering for the $(\text{ZnO})_{1-x}(\text{GaN})_x$ alloy has been predicted to be energetically favorable[6]. Indeed, cluster formation in an alloy is expected to change the optical properties of the alloy, e.g. a decrease in E_g was found for the ZnO-InN system[29]. In our theoretical calculations using the PBE functional, thirty configurations were constructed for $(\text{ZnO})_{1-x}(\text{GaN})_x$ with $x = 0.194$. This composition has been found to be in the steady-bandgap regime $(0.07 \leq x \leq 0.20)$[12], whereas lower concentrations yield strong bandgap bowing. Many of the other alloy configurations have total energies that are substantially higher than the most stable one, and they are therefore not thermodynamically feasible. Thus, the change in the formation energy can be calculated for different configurations of the alloy, so that the change in the formation energy per atom, $\Delta H_f/\text{atom}$, for a specific $x = 0.194$ cell, is given by;

$$\frac{\Delta H_f}{atom} = \frac{E_{Tot}(x = 0.194)_{conf} - E_{Tot}(x = 0.194)_{m.s.}}{72}$$

where $E_{Tot}(x = 0.194)_{conf}$ is the total energy of a configuration, while $E_{Tot}(x = 0.194)_{m.s.}$ is the total energy of the most stable configuration of the $x = 0.194$ cell. The calculated ΔH_f is divided by the number of atoms in the super cell, i.e. 72, to find ΔH_f per atom. In Figure 8, the change in the formation energy per atom is

plotted against the number of Ga-N bonds in the cell. Indeed, there is a decrease in ΔH_f with increasing number of Ga-N bonds, indicating that more Ga-N bonds yield more stable configurations, which also has been found in other studies[4,6,17,30]. This result makes the formation of nano-sized GaN clusters to be a probable consequence of the post-deposition anneals, so that more Ga-N bonds are formed to lower the energy of the system, assuming that Ga and N are sufficiently mobile during the post-deposition annealing to find a more energetically favorable position. This can explain the broadening of the (0002) peak in Figure 6 and the unsystematic variations in the bandgap, (in Figure 7) as different alloy configurations may have different bandgaps superimposed during the measurement. Since the Ga-N and Zn-O bonds have different strengths reflected in different lattice constants, the more Ga-N bonds are formed during the annealing processes, the broader the (0002) reflection is, supporting hypothesis (ii).
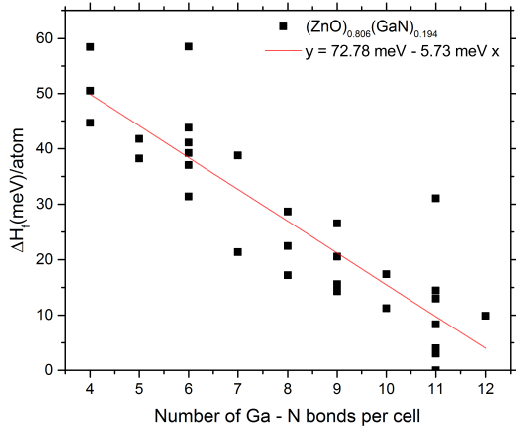
FIG. 8: The calculated change in formation energy per atom, ΔH_f/atom, as a function of Ga-N bonds for $x = 0.194$.

V. CONCLUSION

In conclusion, $(ZnO)_{1-x}(GaN)_x$ thin films with x ranging from 0 to 0.2 were deposited on different lattice-matched substrates. Structurally, the alloy thin films deposited on ZnO substrate yield lowest tensile strain and dislocation density compared to the films deposited on c-sapphire and quartz. Optically, there were no significant variations in either the estimated E_g nor in the size of the Urbach tail among the samples. The films were also post-deposition annealed to investigate the effects of heat-treatment. In the course of anneals, the overall crystalline quality of the films was found to increase, while a significant relaxation in the c-lattice constant was observed, lowering the tensile strain of the films. In addition, the grain size was found to increase with annealing, with the mean values of 20 nm up to 50 nm found for $x = 0.15$ sample before and after annealing respectively, as well as a decrease in dislocation density after annealing. The broadening of the $(ZnO)_{1-x}(GaN)_x$ (0002) diffraction peak indicate that the alloy's crystal structure undergoes a change during the post-deposition annealing, where DFT calculations suggest Ga-N cluster-formation to be responsible for this observation.

[1] A. Janotti and C.G. Van de Walle *Rep. Prog. Phys.*, vol. 72, p. 126501, 2009.

[2] K. Maeda, K. Teramura, D. Lu, T. Takata, N. Saito, Y. Inoue, and K. Domen, "Photocatalyst releasing hydrogen from water," *Nature*, vol. 440, p. 295, Mar. 2006.

[3] J. Liu, M. V. Fernández-Serra, and P. B. Allen, "Special quasiordered structures: Role of short-range order in the semiconductor alloy $(GaN)_{1-x}(ZnO)_x$," *Phys. Rev. B*, vol. 93, no. 054207, pp. 1–8, 2016.

[4] L. L. Jensen, J. T. Muckerman, and M. D. Newton, "First-Principles Studies of the Structural and Electronic Properties of the $(Ga_{1-x}Zn_x)(N_{1-x}O_x)$ Solid Solution Photocatalyst," *J. Phys. Chem. C*, vol. 112, pp. 3439–3446, 2008.

[5] S. H. Wei and A. Zunger, "Role of d states in II-VI semiconductors," *Physical Review B*, vol. 37, pp. 8958–8981, May 1988.

[6] C. D. Valentin, "Electronic Structure of $(Ga_{1-x}Zn_x)N_{1-x}O_x$ Photocatalyst for Water Splitting by Hybrid Hartree-Fock Density Functional Theory Methods," *Journal of Physical Chemistry C*, vol. 114, pp. 7054–7062, 2010.

[7] M. N. Huda, Y. Yan, S.-H. Wei, and M. M. Al-Jassim, "Electronic structure of ZnO:GaN compounds: Assymetric bandgap engineering," *Phys. Rev. B*, vol. 78, no. 195204, 2008.

[8] S. Wang and L.-W. Wang, "Atomic and Electronic Structures of GaN/ZnO Alloys," *Physical Review Letters*, vol. 104, no. 065501, pp. 1–4, 2010.

[9] K. Maeda, K. Teramura, T. Takata, M. Hara, N. Saito, K. Toda, Y. Inoue, H. Kobayashi, and K. Domen, "Overall Water Splitting on $(Ga_{1-x}Zn_x)(N_{1-x}O_x)$ Solid Solution Photocatalyst: Relationship between Physical Properties and Photocatalytic Activity," *The Journal of Physical Chemistry B*, vol. I09, pp. 20504–20510, 2005.

[10] K. Maeda and K. Domen, "Solid Solution of GaN and ZnO as a Stable Photocatalyst for Overall Water Splitting under Visible Light," *Chem. Mater.*, vol. 22, pp. 612–623, 2010.

[11] H. Chen, L. Wang, J. Bai, J. C. Hanson, J. B. Warren, J. T. Muckerman, E. Fujita, and J. A. Rodriguez, "In Situ XRD Studies of ZnO/GaN Mixtures at High Pressure and High Temperature: Synthesis of Zn-Rich $(Ga_{1-x}Zn_x)(N_{1-x}O_x)$ Photocatalysts," *J. Phys. Chem. C*, vol. 114, pp. 1809–1814, 2010.

[12] V. S. Olsen, K. Bazioti, A. Azarov, B. G. Svensson, A. Kuznetsov, O. Prytz, and L. Vines, "Bandgap bowing in $(ZnO)_{1-x}(GaN)_x$ thin films; influence of composition and structural properties," *Semiconductor Science and Technology*, vol. 34, no. 015001, pp. 1–7, 2019.

[13] C. Yang, Y. Hirose, T. Wakasugi, N. Kashiwa, H. Kawai, K. Yamashita, and T. Hasegawa, "Epitaxy of $(GaN)_{1-x}(Zno)_x$ Solid-Solution Thin Films with Widely Tunable Chemical Composition and Strong Visible Absorption," *Phys. Rev. Appl*, vol. 10, no. 044001, pp. 1–9, 2018.

[14] M. Mapa, K. S. Thushara, B. Saha, P. Chakraborty, C. M. Janet, R. P. Viswanath, C. M. Nair, K. V. G. K. Murty, and C. S. Gopinath, "Electronic Structure and Catalytic Study of Solid Solution of GaN in ZnO," *Chem Mater*, vol. 21, pp. 2973–2979, 2009.

[15] J. Li, B. Liu, A. Wu, B. Yang, W. Yang, F. Liu, X. Zhang, V. An, and X. Jiang, "Composition and Band Gap Tailoring of Crystalline $(GaN)_{1-x}(ZnO)_x$ Solid Solution Nanowires for Enhanced Photoelectrochemical Performance," *Inorg Chem*, vol. 57, pp. 5240–5248, 2018.

[16] S. Shet, Y. Yan, J. Turner, and M. Al-Jassim, "Effect of gas ambient and varying RF sputtering power for bandgap narrowing of mixed (ZnO:GaN) thin films for solar driven hydrogen production," *J. Power Sources*, vol. 232, pp. 74–78, 2013.

[17] L. Li, J. T. Muckerman, M. S. Hybertsen, and P. B. Allen, "Phase diagram, structure, and electronic properties of $(Ga_{1-x}Zn_x)(N_{1-x}O_x)$ solid solutions from dft-based simulations," *Phys. Rev. B*, vol. 83, no. 134202, 2011.

[18] J. P. Perdew, K. Burke, and M. Ernzerhof, "Generalized gradient approximation made simple," *Phys. Rev. Lett.*, vol. 77, no. 18, p. 3865, 1996.

[19] J. P. Perdew, K. Burke, and M. Ernzerhof, "Errata: Generalized grandient approximation made simple [phys. rev. lett. 77, 3865 (1996)]," *Phys. Rev. Lett.*, vol. 78, no. 7, p. 1396, 1997.

[20] P. E. Blöchl, "Projector augmented-wave method," *Phys. Rev. B*, vol. 50, pp. 17953–17979, Dec 1994.

[21] G. Kresse and D. Joubert, "From ultrasoft pseudopotentials to the projector augmented-wave method," *Phys. Rev. B*, vol. 59, pp. 1758–1775, Jan 1999.

[22] A. R. Denton and N. W. Ashcroft, "Vegard's law," *Phys. Rev. A*, vol. 43, Mar. 1991.

[23] P. Fons, K. Iwata, S. Niki, A. Yamada, and K. Matsubara, "Growth of high-quality epitaxial ZnO films on α-Al_2O_3," *Journal of Crystal Growth*, vol. 201-202, pp. 627–632, 1999.

[24] Y. Chen, D. M. Bagnall, H.-J. Koh, K.-T. Park, K. Hiraga, Z. Zhu, and T. Yao, "Plasma assisted molecular beam epitaxy of ZnO on c-plane sapphire: Growth and characterization," *Journal of Applied Physics*, vol. 84, no. 7, pp. 3912–3918, 1998.

[25] D. Singh, R. Kumar, T. Ganguli, and S. S. Major, "High resolution x-ray diffraction study of the substrate temperature and thickness dependent microstructure of reactively sputtered epitaxial ZnO films," *Materials Research Express*, vol. 4, no. 9, 2017.

[26] M. A. Moram and M. E. Vickers, "X-ray diffraction of III-nitrides," *Reports on Progress in Physics*, vol. 72, no. 036502, pp. 1–40, 2009.

[27] P. Scherrer, "Bestimmung der Grösse und der inneren Struktur von Kolloidteilchen mittels röntgenstrahlen," *Nachrichten von der Gesellschaft der Wissenschaften zu Göttingen*, pp. 98–100, 1918.

[28] K. Maeda, K. Teramura, and K. Domen, "Effects of post-calcination on photocatalytic activity of $(Ga_{1-x}Zn_x)(N_{1-x}O_x)$ solid solution for overall water splitting under visible light," *Journal of Catalysis*, vol. 254, pp. 198–204, 2008.

[29] M. Dou, G. Baldissera, and C. Persson, "ZnO-InN nanostructures with tailored photocatalytic properties for overall water-splitting," *Int. J. Hydrogen Energy*, vol. 38, pp. 16727–16732, 2013.

[30] J. Liu, L. S. Pedroza, C. Misch, M. V. Fernández-Serra, and P. B. Allen, "Temperature and composition dependence of short-range order and entropy, and statistics of bond length: the semiconductor alloy $(GaN)_{1-x}(ZnO)_x$," *J Phys : Condens Matter*, vol. 26, no. 274204, pp. 1–9, 2014.

Supplemental Materials

The supplementary materials includes data that has not been included in the main article. Structurally, TEM images, RBS measurements and the measured FWHM from the rocking curve scans are included.

Figure S1 illustrates the $(ZnO)_{0.85}(GaN)_{0.15}/Al_2O_3$ heterostructure recorded under two-beam conditions with g0002 (a) before and (b) after post-deposition annealing. It is evident that in the case of the as-grown sample there is a high density of c-type TDs that is clearly decreased after annealing. It is worth noting that the comparison was made in areas having the same thickness along the viewing direction. The thickness was evaluated working in EELS-STEM, according to the $t/\lambda = \ln(I_t/I_0)$, where t is the thickness, λ the inelastic mean free path, I_t the intensity of the entire spectrum and I_0 the intensity of the zero loss peak. Figure S2 illustrates a high-resolution HAADF-STEM
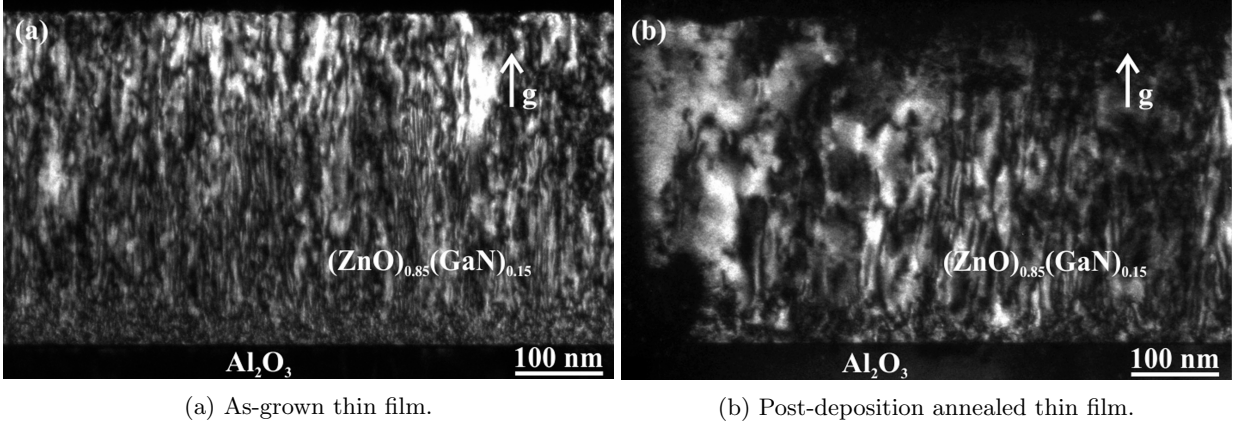

(a) As-grown thin film.

(b) Post-deposition annealed thin film.

FIG. S1: The $(ZnO)_{0.85}(GaN)_{0.15}$ composition measured using the weak-beam dark field g/3g method to investigate the dislocation density.

image of the $(ZnO)_{0.85}(GaN)_{0.15}$ thin film deposited on Al_2O_3 substrate after annealing at 800 °C, recorded along the $[11\bar{2}0]$ zone axis. By comparing this film wo the as-grown one (not shown here), the stacking sequence along the [0001] direction is retained following the ABABAB stacking of the hexagonal structure after annealing, indicating no structural change. Furthermore, imaging in both TEM and STEM-mode did not reveal any Moiré fringes. Since in HAADF-STEM image the intensity is proportional to the atomic number and the thickness of the sample, the dark areas correspond to areas with lower Z. RBS measurements in random and channeling modes were undertaken for the $x = 0.15$ as-deposited and annealed samples, see Figure S3. The depth scale of 3.8 nm/channel is also depicted in the figure. Notably, the density of the films was assumed to be similar to pure ZnO (8.3×10^{22} at/cm^3) and the depth scale was found to be identical for Zn and Ga atoms due to similarity in masses. The channeled spectra for the 800°C annealed film (blue) almost resembles the as-grown one, indicating that the thermal heat treatment does not lead to a substantial improvement of the disorder, as measured by RBS. In turn, minor changes can be attributed to the defect reconstruction and increase in grain size as clearly demonstrated by TEM results.

As for the rocking curve scans, the FWHM of the rocking curve scans was measured after each annealing step (as-grown, annealed at 600°C, 700°C and 800°C). The measured FWHM for the different compositions as a function of annealing temperature can be seen in Figure S4.

Optically, the measured transmittance for $x = 0.0$, $x = 0.02$ and $x = 0.15$ can be seen as a function of wavelength in Figure S5.
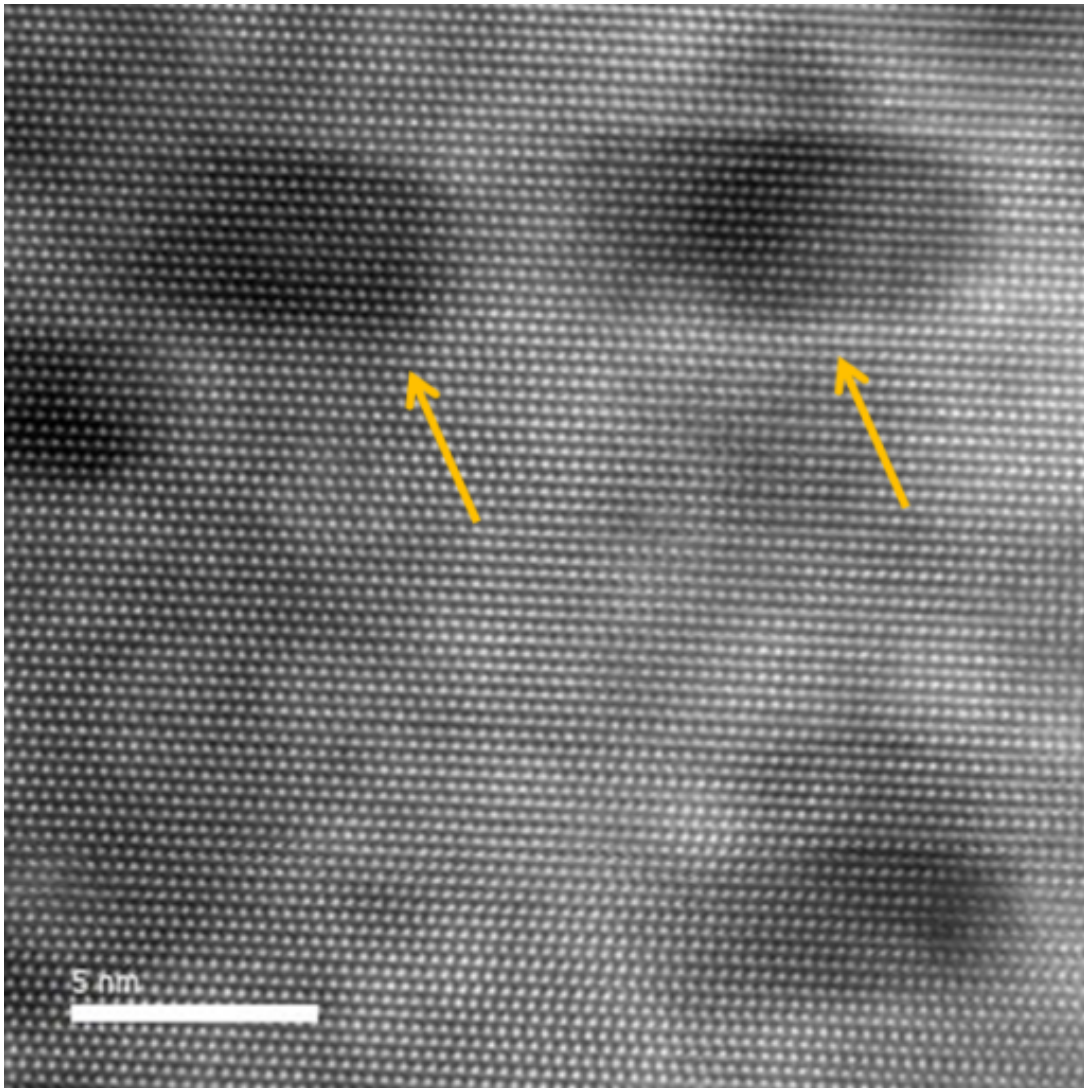
FIG. S2: High-resolution HAADF-STEM image along the $[11\bar{2}0]$ z.a. of the $(ZnO)_{0.85}(GaN)_{0.15}$ thin film on Al_2O_3 substrate after annealing at 800 °C. The yellow arrows marks the voids observed in the films.
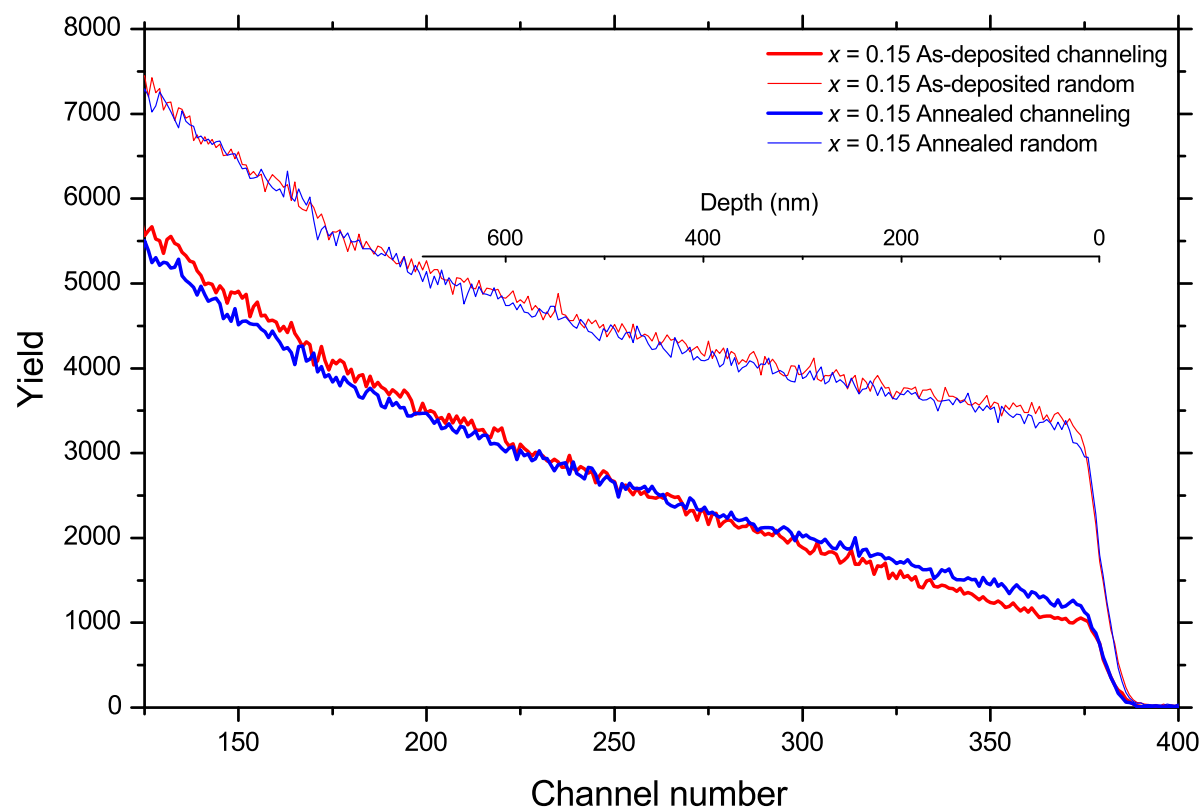
FIG. S3: RBS spectra acquired in random and channeling modes. The thick lines represent measurements done in channeling mode, while the thin ones represent random mode. The film surface is at channel 379, and the depth scale is included in the panel.
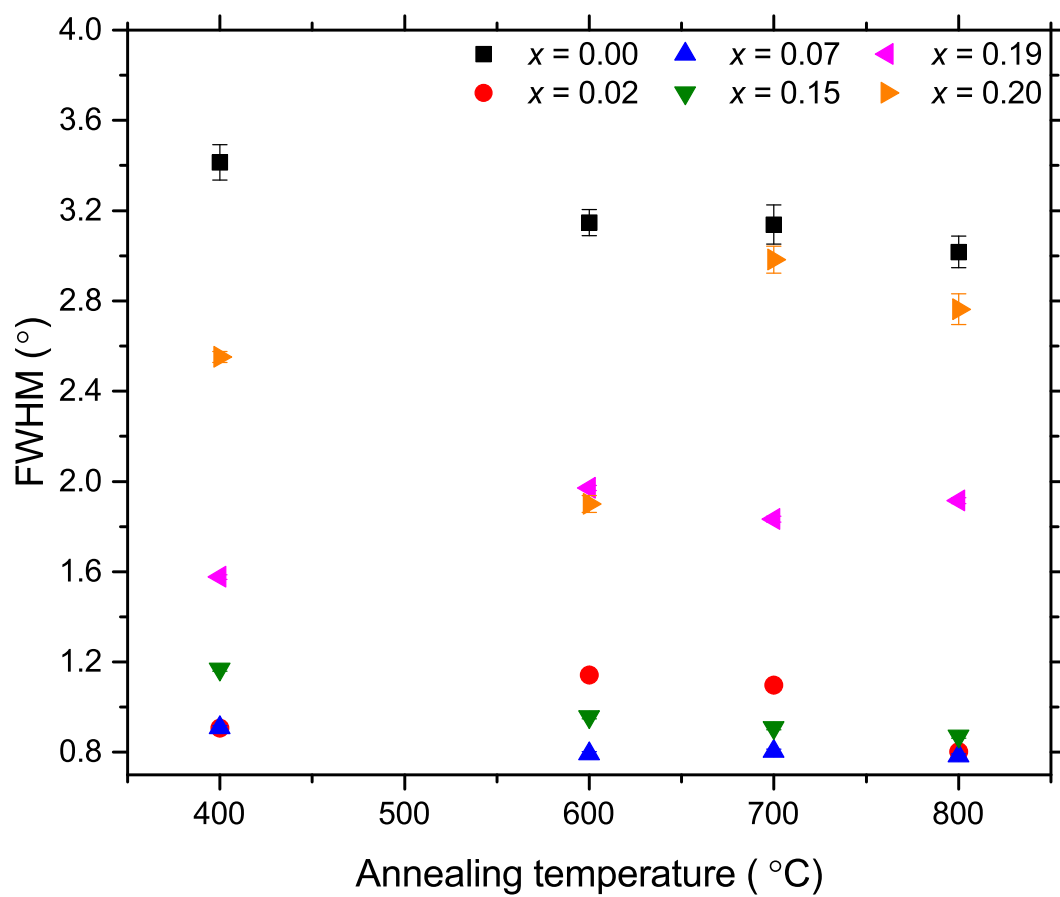
FIG. S4: FWHM of the (0002) reflection measured with rocking curve scans as a function of post-deposition annealing temperature for different alloy compositions.
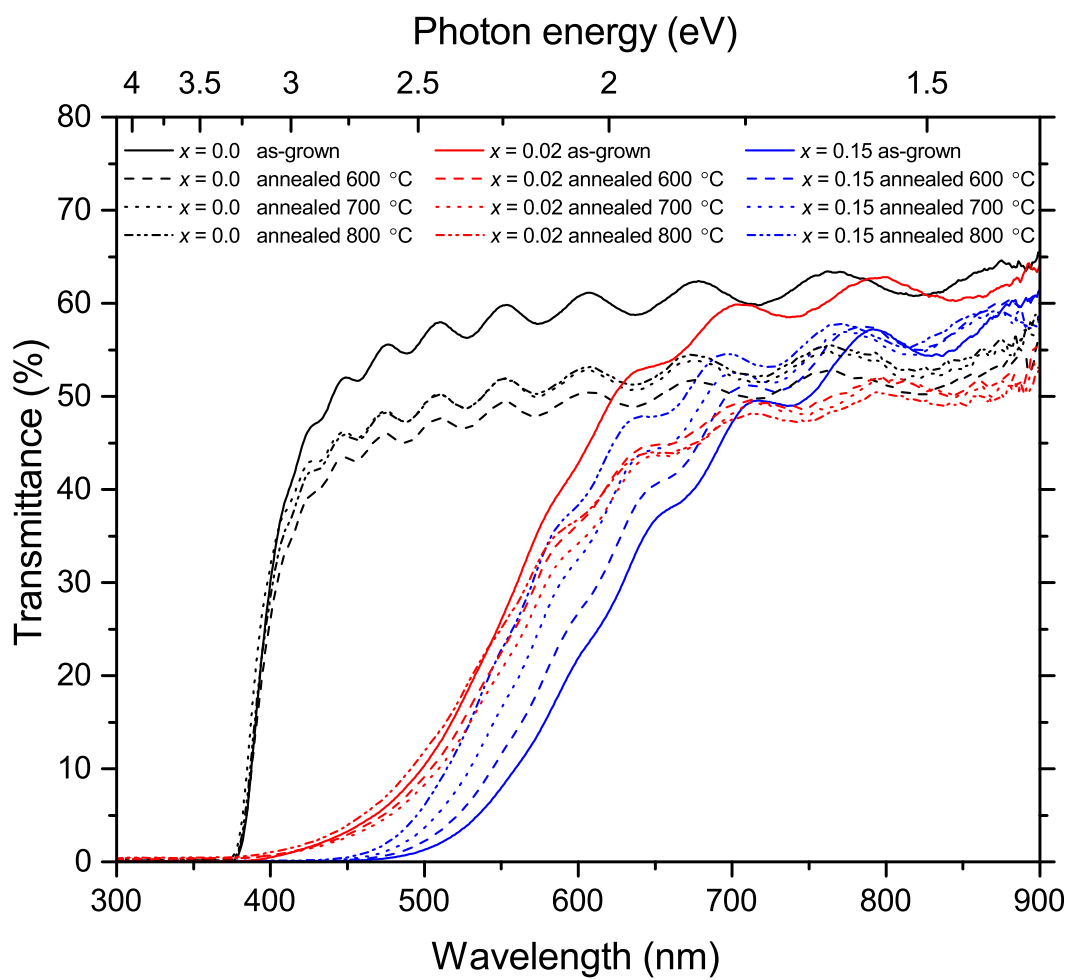
FIG. S5: Measured transmittance as a function of wavelength for three compositions $x = 0.0$, 0.02 and 0.15.